Journal of Photochemistry & Photobiology, A: Chemistry 444 (2023) 114916

Contents lists available at ScienceDirect

Journal of Photochemistry & Photobiology, A: Chemistry

journal homepage: www.elsevier.com/locate/jphotochem

Oxygen vacancies in the Spotlight: On the engineering of intrinsic defects in highly defective TiO_2 photocatalysts

Daniela Meroni [a,b], Carolina Cionti [a], Lucia Silvestrini [c], Noga Gal [d], Marco Cazzaniga [a], Michele Ceotto [a], Giacomo Buccella [e], Leonardo Lo Presti [a,f,*], Giuseppe Cappelletti [a,b]

[a] Università degli Studi di Milano, Dipartimento di Chimica, Via Golgi 19, 20133 Milano, Italy
[b] Consorzio INSTM, via Giusti 9, 50121 Florence, Italy
[c] Institute of Microbial Genetics, Department of Applied Genetics and Cell Biology, University of Natural Resources and Life Sciences (BOKU), Konrad Lorenz Straße 24, 3430 Tulln an der Donau, Austria
[d] Department of Bionanosciences, University of Natural Resources and Life Sciences (BOKU), Muthgaße 11/II, 1190 Vienna, Austria
[e] Politecnico di Milano, Department of Chemistry, Materials and Chemical Engineering "Giulio Natta", Piazza Leonardo da Vinci 32, Milano, Italy
[f] Istituto Nazionale di Fisica Nucleare (INFN), Laboratori Nazionali di Frascati, Frascati, Italy

A B S T R A C T

Nanostructured oxide semiconductors are widely used in energy conversion, catalysis, sensing and environmental applications, due to their high stability, commercial availability, efficiency and low cost. Despite its crucial importance for the design of more efficient materials, the interplay between intrinsic and extrinsic defects is yet to be clarified. For example, oxygen vacancies (V_O's) can be either beneficial or detrimental to the desired performances, depending on a variety of factors. Here, we synthesize TiO_{2-x} samples by the addition of three different N chemical sources (NH_3, triethylamine, urea). X-ray absorption spectroscopy, confocal microscopy, UV–vis absorbance and fluorescence, are employed to explore the occurrence and location of V_O's both in real and energy spaces. High–grade bulk DFT simulations complement the experimental picture. Synergy between theory and experiment, on the one hand, estimates the relative V_O's content in the different samples from local structural information. On the other hand, a sharp optical transition at ≈2.7 eV serves an unequivocal spectral signature of bulk V_O's, allowing a semi-quantitative analysis by confocal microscopy. Surface oxygen vacancies do not display fluorescence features under UV pumping, possibly due to the reaction of surface defects with atmospheric O_2. Thus, the comparison between local structure and confocal microscopy can discriminate surface-localized and bulk V_O's. Concurrently, UV-induced photochromism and visible light photodegradation shed light on the most effective reactive defects. Eventually, surface-localized oxygen vacancies are predominant where actual N substitutional doping occurs, leading to materials exhibiting visible-light activity and characteristic photochromic behaviour. Implications on strategies for concomitant V_O engineering and extrinsic doping are discussed.

1. Introduction

Oxide-based semiconductor materials are at the forefront of innovative technologies for pollutant remediation, renewable energy production and storage, optoelectronics, sensing and CO_2 reduction. [1–6] Being cheap, stable and highly versatile, as their properties can be tuned by adjusting the synthesis procedure [7] and doping strategies [8–10], oxide semiconductors are well-suited for large–scale industrial applications.

It is widely acknowledged that the intrinsic and extrinsic defectivity of semiconductor oxides plays a pivotal role in determining their physicochemical properties and ensuing performance. In particular, oxygen vacancies (V_O's) are key players in determining the surface and bulk properties of semiconductor oxides, from adsorption behaviour to their electronic features. [11–12] As a result, growing interest is being paid to strategies to control the V_O concentration and distribution. [13–18] For instance, highly defective TiO_{2-x} materials have been extensively investigated to develop efficient photocatalysts, especially under visible-light irradiation. The most common synthesis protocols include thermal treatment with H_2, [15] reduction with $NaBH_4$ [18] and doping with accurately chosen extrinsic species. [17].

Unfortunately, there is still an incomplete understanding on the interplay of different defects in determining the final material performance. [12] A case in point is represented by TiO_{2-x} materials, where V_O's play a Jekyll-and-Hyde role. To ensure electroneutrality, V_O's are accompanied by charged defects, like reducing Ti^{3+} centres. [19] The latter are associated to shallow mid–gap states [20] that lower the apparent band gap and shift the main absorption edge into the visible region. Moreover, V_O's increase the oxide adsorption properties, especially if they lie close to the oxide–solution interface. [14,21] These

* Corresponding author at: Università degli Studi di Milano, Dipartimento di Chimica, Via Golgi 19, 20133 Milano, Italy.
E-mail address: leonardo.lopresti@unimi.it (L. Lo Presti).

https://doi.org/10.1016/j.jphotochem.2023.114916
Received 10 March 2023; Received in revised form 27 May 2023; Accepted 5 June 2023
Available online 8 June 2023

merits clash against a faster electron–hole (e^-–h^+) recombination, [22] as the same V_O's act as recombination centres that lower the lifetime of photogenerated e^-–h^+ pairs. As a result, developing oxides with optimized performance is often a matter of trial and error.

The reasons for this lack of knowledge are twofold. First, techniques able to quantify the amount of V_O's are not available, especially in the presence of dopants and/or multiphasic systems. Titania defects, such as V_O's, can be studied through X-ray photoelectron spectroscopy (XPS), X-ray absorption spectroscopy (XAS), reverse double beam photoacustic spectroscopy, [23] wet-chemical electron trap titration methods, [24–25] and electron paramagnetic resonance (EPR) spectroscopy, [26–28] which try to provide tentative quantifications but cannot easily discriminate among the various kinds of defects in complex matrices. Second, a further issue is the location of V_O's defects, since bulk and surface species have different effects on adsorption and recombination phenomena. [12,29] For instance, Cao et al. recently studied the influence of surface vacancies by transmission electron microscopy (TEM) and electron energy loss spectroscopy (EELS), in enhancing the photocatalytic activity of TiO_2 towards Rhodamine B degradation and hydrogen generation. [27]In any case, the occurrence of significant amounts of bulk defects can be expected, especially at high dopant concentrations. [30] Doping by heteroatoms, such as N species, is thought to promote the formation of extra oxygen vacancies to ensure lattice electroneutrality. According to the Kröger–Vink notation, the equilibrium is:

$$\frac{1}{2}O_2 + 2N_O^{'} + V_O^{\bullet\bullet} \rightleftharpoons N_2 + O_O \quad (1)$$

In (1), $N_O^{'}$ stands for substitutional nitrogen and $V_O^{\bullet\bullet}$ is the oxygen vacancy, while O_O corresponds to an oxygen sitting on the expected crystallographic site. The charge states of the various defects are represented by apices, with apostrophe (') and dot (·) meaning negative and positive charges. Thus, 1 mol of oxygen vacancies is needed to compensate 2 mol of substitutional nitrogen. However, the amount of defects is highly dependent also on the synthesis method, and particularly on the nitrogen precursor selected. It has been proposed that when ammonia or urea is adopted as N precursors during wet syntheses of TiO_2, the formation of labile NO-TiO_2 species [31] or of heterojunctions with g-C_3N4 [32] may preferentially occur instead of N-doping. In a recent review, Pulgarin and coauthors called for more studies to explore these issues. [31].

This work aims to shed light on the interplay between oxygen vacancies and N species in TiO_{2-x} materials prepared using different N precursors (ammonia, triethylamine and urea). Their role on the optical, photochromic and photocatalytic properties of the resulting materials is discussed. Probes ranging from X-ray to UV–vis light, including X-ray absorption spectroscopy, confocal fluorescence microscopy, UV–vis absorption and fluorescence spectroscopy, are combined with high-grade DFT simulations to locate V_O centres both in the real and energy spaces. By this innovative approach, we disentangled the effects related to surface-localized V_O's defects in this complex, multi-defect systems.

2. Materials and methods

2.1. Synthesis of TiO_2 materials

All reactants were purchased from Sigma-Aldrich and used without further purification. Solutions and suspensions were prepared using doubly distilled water passed through a Milli-Q apparatus. Pristine and N-modified TiO_2 samples were synthesized by a sol–gel route using titanium (IV) isopropoxide (TTIP) as starting material and three different N-containing species (triethylamine, ammonia and urea) as N-sources. TTIP (30.7 mL) and 2-propanol (37.6 mL) were mixed in a 500 mL flask. Then, 180 mL of a basic solution containing KOH and a variable amount of N species was added dropwise while stirring at 300 rpm. The concentration of the basic solution was adjusted to fix the pH at 9. The adopted H_2O/TTIP and H_2O/2-propanol molar ratios were 100 and 20, respectively. The obtained gel was stirred for 90 min, then dried in oven at 80 °C overnight. Finally, the powder was calcined at 400 °C for 6 h under O_2 stream (9 normal liters per hour).

Titania samples prepared with the addition of triethylamine (-T), urea (-U) and NH_3 (-N) are named "TNT_x", "TNU_x" and "TNN_x", respectively, with × standing for the nominal N/Ti molar ratio (x = 0.1 and 0.5), whereas the pristine one is labelled as "T".

2.2. Materials characterization

Powder X-ray diffraction (PXRD) patterns were collected using graphite-monochromated Cu Kα radiation on a Philips PW 3710 Bragg-Brentano goniometer equipped with a scintillation counter and 1° divergence slit, 0.2 mm receiving slit and 0.04° Soller slit systems. Scans were recorded at 40 kV × 40 mA nominal X-rays power between 20° and 90°, using a step size 0.1° wide. Instrumental line broadening effects were corrected using a microcrystalline Si-powdered standard. The average crystallite size for the anatase phase was determined applying the Scherrer equation to the (1 0 1) most intense non-overlapping reflection attributed to this phase.

The specific surface area of the samples was characterized by adsorption–desorption isotherm of N_2 in subcritical conditions using the Brunauer–Emmett–Teller (BET) method on a Coulter SA3100 apparatus. Total pore volume was determined from desorption isotherms using the Barrett-Joyner-Halenda (BJH) method.

Diffuse reflectance spectroscopy (DRS) measurements were carried out on a Shimadzu UV-2600 UV–vis spectrophotometer, equipped with an integrating sphere. Spectral scans were performed in the 250–700 nm range, using $BaSO_4$ as a reference. Apparent band gap values, E_g, were determined according to the Kubelka-Munk method. [33] Spectral measurements were carried out before and after irradiation with UV, using a Jelosil HG500 halogen lamp with an effective power density of 17.0 mW cm^{-2} between 280 and 400 nm. To ensure the reproducibility of the measurements and avoid inhomogeneous irradiation of the powder samples due to light penetration effects, the DRS sample holder was packed with a proper amount of ground and homogenized powder to prepare a compact, flat and homogeneous surface. The sample was then analyzed with the spectrophotometer, irradiated without removing it from the sample holder and remeasured at set time intervals.

Extended X-ray absorption fine structure (EXAFS) spectra were recorded at the Swiss-Norwegian beamline (BM01B) at the European Synchrotron Radiation Facility (ESRF). The TiO_2 powder was diluted in $CaCO_3$ to avoid thickness effects. X-ray absorption curves were collected in transmission mode across the Ti K-edge at room temperature. A Si (1 1 1)-monochromated beam was employed, either in the 4.9–5.4 keV (pure TiO_2) or in the 4.9–5.8 keV (TNN, TNU and TNT series) energy ranges. The Horae suite of programs, [34] based on the IFEFFIT library, [35] was used throughout for data processing and fitting, adopting the same strategy described in detail elsewhere. [30] Section S1 in the Supporting Information summarizes the details of the least-squares fittings.

UV–Vis fluorescence spectra were recorded with a LS55 fluorescence spectrophotometer on water-suspended nanostructured TiO_2 powders. Two scan modes were employed. In the "excitation" (EX) one, the spectral intensity was monitored as a function of the pumping wavelength, looking at a fixed fluorescence emission of 2.254 eV (λ = 550 nm). In the "emission" (EM) mode, the excitation wavelength was fixed at 3.179 eV (λ = 390 nm), which corresponds to the maximum of the EX scan. Then, the fluorescence intensity was probed as a function of the emitted wavelength. Raw spectral data were normalized according with the procedure proposed by Angulo and co-workers. [36].

Images of TNN, TNU and TNT samples were acquired by confocal laser scanning microscope (CLSM) Olympus FV1000. A spot of 1000x diluted TiO_2 nanoparticles, previously vortexed and heated, was aliquoted on a microscopy glass. More in detail, an aliquot of the water-

suspended nanoparticles stock (1:1 v/v) was diluted in distilled water in order to observe an appreciable decrement of nanoparticle aggregates. The best resulting dilution of the nanoparticles stocks was 1000x. Then, 5 μL were put on a laboratory slide and analyzed. Great care was taken to optimize the operational parameters of the laser and the detector. Excitation was performed at the lowest wavelength achieved by the microscope (405 nm). The detector voltage was initially set at 580 V, which allowed us to consider luminescence of pristine TiO_2 nanoparticles close to zero, the calibration state for the quantification of emission related to N addition. As indicated below, the detector voltage was incremented to 700 V, due to the unexpected background luminescence of pristine TiO_2 nanoparticles which could be due to intrinsic material defects. This increment enables to detect the minimal luminescence of particles by keeping a low laser intensity (10%). When the laser intensity was increased to 12.9%, the fluorescent spots could be clearly appreciated (Figures S10–S12), but without an accurate determination of the intensities, as the photon flux overcame the linearity interval of the detector. A lower laser intensity, coupled with a lower sample loading, was deemed necessary to quantify the fluorescence intensity by microdensitometry. The microscope ouverture was set at 4x and the offset values within the range of 30–50%. Particles detected on each image were counted by Image J Fiji software [37] and the related luminescence intensity was calculated.

Confocal microscopy is sensitive to the distribution of active fluorophores within the bulk volume of each independent crystal lattice. However, in the present case, samples are aggregates of nanostructured particles (Figures S10–S12), which have μm-to-mm large thickness and can shield the fluorescence output effectively. Moreover, both total integrated intensity and self-absorption depend on the amount of material in the active eyepiece area. To provide quantitative estimates, as well as reliable comparisons among different materials, we define a fluorescence density output, I_D as:

$$I_D = \frac{I_{int}}{A_{lum}} \tag{3}$$

and a total specific fluorescence, I_S according to:

$$I_s = \frac{I_{int}}{A_{tot}} \tag{4}$$

where I_{int} is the total integrated fluorescence intensity (in arbitrary units) as retrieved from the visible blue spots of each image, A_{lum} is the corresponding total emitting area and A_{tot} the total area covered by nanoparticle aggregates (in μm^2). I_D represents the average emitting density per unit area. It is easy to see that the I_S/I_D ratio corresponds to the A_{lum}/A_{tot} ratio, that is, to the relative amount of emitting area with respect to the total area. As extrinsic and intrinsic defects are expected to be distributed randomly through each whole nanostructured powder, we propose to take the quantity $\omega = 1 - A_{lum}/A_{tot} = 1 - I_S/I_D$ as a measure of the self-absorption due to aggregation of the nanoparticles.

2.3. Photocatalytic tests

The photocatalytic activity of the samples was tested towards the gas phase degradation of a model volatile organic compound (ethanol) under either UV (Jelosil HG500 halogen lamp) or visible light (Lot Oriel halogen lamp equipped with a 400 nm long wave pass edge filter). Effective power density values during photocatalytic tests at sample distance were determined using a Thorlabs S314C radiometer and were 17.0 and 2.4 mW cm^{-2} for UV and visible light irradiation, respectively. The adopted photocatalytic apparatus was described previously [38] and consists of a 5 L batch reactor with diameter of 200 mm filled with dry air from gas cylinders. The reaction was monitored via a gas-chromatographic system (Agilent 7890 equipped with Porapak and DB-VAX columns, a methanator and two FID detectors), following both ethanol disappearance, intermediate formation (acetaldehyde) and build-up of CO_2 as mineralization final product. The TiO_2 powders were drop casted on a glass Petri dish: 50 and 70 mg of sample powder, corresponding to an irradiated area of 51 and 102 cm^2, were used respectively for UV and visible tests due to the different reaction rates provided by the two irradiation sources. An ethanol starting concentration of 238 ppm was employed for all tests.

2.4. DFT simulations

Theoretical simulation were performed with the ab initio plane-wave Quantum-Espresso (Q-E) suite [39–41] with a PBE + U level of theory. For the Hubbard U splitting we choose a value of 3.5 eV since it provides a compromise between the increasing band gap and preserving lattice parameters comparable with experiment. [42–43] The core electrons are accounted by ultrasoft pseudopotentials and we set the energy cutoff to 50 Ry for the wavefunctions and 400 Ry for the electron density. We obtained the theoretical lattice parameters of anatase by performing a variable cell optimisation with a $10 \times 10 \times 10$ k-points mesh obtaining a lattice parameter a = 3.838 Å and c = 9.711 Å (reasonably close to the experimental values of a = 3.782 Å and c = 9.502 Å) [44] with an electronic band gap of 2.477 eV (still smaller than the experimental value of 3.2 eV). [44] The supercell has been generated by $3 \times 3 \times 1$ replicas of the conventional cell and, consequently, the k-points sampling was reduced to a $2 \times 2 \times 2$ mesh for the supercell. The resulting vacancy concentration in our model is 7.8 10^{20} cm^{-3}. This value is a tradeoff between computational costs and accurately modeling V_O's independent from each other. We do not expect significant changes in the electronic structure for lower V_O's concentrations. Since the removal of an oxygen atom in the supercell yields to a pair of excess electrons, all the calculations have been performed with a collinear spin polarization (unrestricted DFT) with the orbital occupation described adopting a gaussian smearing of 0.005 Ry. We tested several starting guesses, eventually identifying the most stable spin configurations (both with parallel and antiparallel spins). We found a substantial agreement with previously published results. [19,45–50] For the detected states we analyzed the Spin Density, total Density of States (DOS), its Projection on selected atoms (PDOS), and computed the Bader charges. To achieve reliable results for the DOS we increased the *k*-point sampling adopting a $5 \times 5 \times 5$ mesh. Finally, the Bader analysis have been performed thanks to the Critic2 code [51–52] starting from the electron density obtained from the Q-E code.

3. Results

3.1. Structural and optical properties

Table 1 reports the main physicochemical properties of the prepared samples: in all cases, anatase-brookite composites were obtained, as expected on the grounds of the adopted synthetic conditions and calcination temperature, with N addition favouring a higher anatase content, in agreement with previous reports. [7] The addition of ammonia also promotes the sample crystallinity, almost doubling the anatase crystallite size. [7] Upon N addition, samples exhibit a lower surface area and porosity compared to the pristine reference, especially in the case of urea addition, fully in accordance with the literature. [53].

Moreover, N addition also induces a visible light absorption in all tested samples, [30,53] although the optical properties vary with the type of N source adopted, as shown by Fig. 1. Ammonia and urea give rise to a localized absorption centred around 2.65 eV, with no appreciable shift in the absorption edge (as shown by the derivative graph, Fig. 1, inset). As a result, the apparent band gap value is hardly modified with respect to the pristine reference (Table 1). Increasing the urea content promotes the visible light absorption, whereas no changes are observed in the case of ammonia, probably because of the high volatility of NH_3 and partial oxidation to NO_x (during the calcination step in oxidizing conditions) which may limit the effective amount of N species

Table 1
Physicochemical characteristics of the synthesized TiO_2 samples (phase composition: A for anatase, B for brookite; phase composition (%); average anatase crystallite size, $d_a^{(101)}$; specific surface area, S_{BET}; total pore volume, V_{pores}; apparent band gap value, E_g) and their photocatalytic performance during UV and visible tests in terms of pseudo-first order kinetic rate constant of ethanol degradation, k, and $\%CO_2$ evolved after 30 min of reaction.

sample	PC %	$d_a^{(101)}$ (nm)	S_{BET} ($m^2\ g^{-1}$)	V_{pores} ($mL\ g^{-1}$)	E_g (eV)	photocatalytic tests		
						$k_{EtOH,UV}$ ($x10^3\ s^{-1}$)	$\%CO_{2,UV}$ (30 min)	$k_{EtOH,vis}$ ($x10^4\ s^{-1}$)
T	A: 73 B: 27	6	173	0.240	3.23	70 ± 2	84.7	1.6 ± 0.4
TNN 0.1	A: 85 B: 15	11	112	0.152	3.23	69 ± 2	77.1	1.7 ± 0.4
TNN 0.5	A: 95 B: 5	14	113	0.163	3.23	99 ± 5	94.7	3.9 ± 0.2
TNU 0.1	A: 84 B: 16	9	70	0.071	3.18	66 ± 1	51.6	3.1 ± 0.3
TNU 0.5	A: 88 B: 12	9	53	0.090	3.20	56 ± 1	14.2	1.4 ± 0.4
TNT 0.1	A: 85 B: 15	8	154	0.191	3.06	70 ± 3	74.5	13.8 ± 0.6
TNT 0.5	A: 90 B: 10	9	100	0.029	3.00	54 ± 1	14.4	6.4 ± 0.6

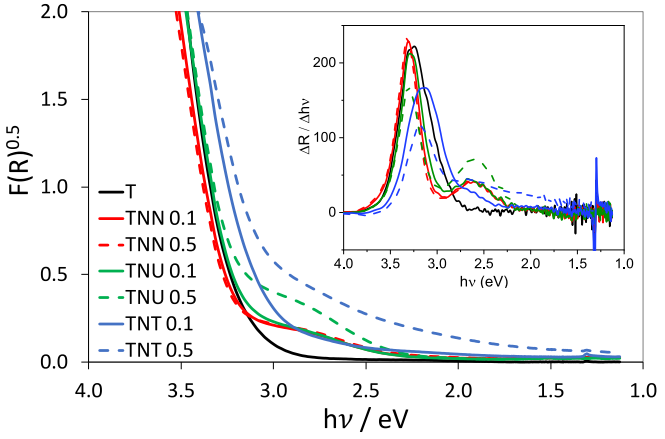

Fig. 1. Kubelka-Munk graph as a function of light energy for the synthesized TiO_2 samples. Inset: Relative first derivative of DR spectra.

introduced.

Visible light sensitization upon urea addition has been attributed to the formation of g-C_3N_4 during calcination at temperatures >350 °C. [32] According to the literature, [54] it is known that g-C_3N_4 gives rise to intense bands in the 1200–1600 cm^{-1} region, in particular, bands at 1250, 1330, 1400, and 1530 cm^{-1} related to the stretching vibration mode of CN heterocycles.

In the present case, however, TNU samples do not exhibit any additional IR features in the 1200–1600 cm^{-1} region compared to the pristine TiO_2 sample, even at the highest tested urea content (Figure S1 in the Supporting Information). This observation is consistent also with photocatalytic data (see Section 3.6).

The addition of triethylamine provokes instead a red-shifted absorption edge, lowering the apparent band gap (Table 1). Furthermore, TNT samples present also a broad absorption in the visible range, more clearly appreciable in the TNT0.5 sample (Fig. 1).

3.2. Local structure

The local structure of the synthesized materials was investigated by EXAFS spectroscopy, which is sensible to the average short-range structure of the probed absorbing atom, particularly to the first coordination shell. In the present case, any distortion from the expected crystallographic anatase structure, which is based on axially elongated TiO_6 octahedra, can be attributed to synthesis-induced lattice defects

Table 2
Average axial and equatorial Ti–O distances as a function of the nominal N/Ti ratio, as estimated from the least squares against EXAFS data on TiO_2 samples. Results for the TNT series are the same already reported in ref. [55]. Estimated standard deviations (e.s.d.'s) in parentheses. See Section S1 for details of the least-squares fittings.

N/Ti nominal ratio	axial			equatorial		
0	2.04(2)			1.82(1)		
	TNT	*TNN*	*TNU*	*TNT*	*TNN*	*TNU*
0.1	2.04 (2)	2.05 (5)	2.08 (5)	1.81 (1)	1.84 (2)	1.80 (2)
0.5	1.93 (3)	2.07 (5)	2.06 (6)	1.83 (1)	1.85 (2)	1.83 (3)

(Table 2). Owing to the nanometer-size distribution of the samples, we focused just on point defects, which imply substitutional N (N_O), interstitial N (N_i) and oxygen vacancies (V_O). We relied upon periodic quantum simulations to disentangle the different structural effects triggered by the various defects, according to a previously reported approach [30]. While N_O's leave unchanged the average Ti–O coordination distances, N_i's lengthen them by up to 5–6%. The reason is that the Ti site symmetry is poorly perturbed by a N_O defect, while N_i produces η^2 coordinated N=O species that strongly distort the local Ti environment. On the contrary, V_O's determine an apparent ≈ 3% shrinkage of the average Ti–O distances. In all cases, the longest axial bonds are the most affected Ti–O distances. Keeping in mind these scenarios, Table 2 reports the average Ti–O first coordination distances as a function of the nominal N/Ti content.

The average equatorial distances are reasonably close to the crystallographic reference [56] and remain unchanged at increasing N precursor amounts. In contrast, the trend of axial distances depends on the N chemical source. At high N concentrations, TNT samples present a significant amount of oxygen vacancies, [30] as it can be appreciated by the apparent reduction of the average Ti–O bond length. This is not the case for urea and ammonia, where axial Ti–O distances remain equal to the pristine reference within 1 estimated standard deviation. Thus, no patent distortions are detectable in the average local TiO_6 structure. This implies that the urea- and ammonia-derived materials do not bear any marked V_O excess compared to the pristine TiO_2.

3.3. Photochromism

The photochromic properties of TiO_2 samples were studied to

investigate the nature of light-active trap centres in the three series of samples. Photochromism is normally interpreted in terms of light-induced formation of charge carriers, followed by their separation at electron and hole traps, thermally-stimulated detrapping and recombination. [57].

Fig. 2 reports differential spectra of the synthesized samples obtained as difference between the reflectance (R) curves of the same sample before and after irradiation with broadband UV light.

Following Serpone and coworkers, [58] the transmittance of titania samples can be safely assumed to be zero, being them opaque to visible light. In Fig. 2, a positive peak means an increase in absorbance (A) upon treatment with UV light, whereas a negative peak implies a corresponding decrease in absorbance. We denote with the as R_0 and R_{irr} the reflectance respectively before and after the UV irradiation process. Then, $R + A = 1$ and $\Delta R = R_0 - R_{irr} = (1–A_0) - (1–A_{irr}) = A_{irr}–A_0$. If $\Delta R > 0$, it follows that $A_{irr} > A_0$, that is, the irradiated sample absorbs more than the not-irradiated one. An increase in light absorption upon UV irradiation is appreciable for most of the samples, especially at the highest N/Ti ratio. This suggests that the number of absorbing defects is growing, whereas a decrease in absorbance implies photobleaching. [54] The pristine sample T shows no change in light absorption after UV irradiation. This implies that photochromism is not due to the intrinsic electronic properties of TiO_2.

A fitting of the differential spectra was performed using Gaussian curves [59] and peak positions, along with peak width and relative area, are reported in Table 3. Details of the fitting procedures and deconvoluted spectra are reported in the Supporting Information (Figure S3).

Also in this case, the TNN and TNU samples exhibit similar behaviour, showing two main components at around 3.0 and 2.2 eV (the latter being the most intense), which imply an improved absorption in the violet (430 nm) and green (530 nm) regions. Conversely, TNT samples show a more complex behaviour. Besides a positive component at ca. 2.9 eV, TNT0.1 is the only specimen that shows a patent broad decrease in absorbance in the 1.8–2.6 eV range (Fig. 2a), *i.e.* in the 690–480 nm (red-blue) region of the visible window, with the minimum lying at 2.3 eV (539 nm). This feature indicates that only UV irradiation reduces the amount of trapped electrons for TNT0.1. On the other hand, TNT0.5 presents all positive peaks, with main components at ca. 2.0 and 1.5 eV (Fig. 2b).

Overall, these data suggest a similar nature and content of trap defects in TNN and TNU samples, supporting also a lesser role of the nominal N/Ti ratio on the former. Moreover, in good agreement with EXAFS data, photochromic spectra show the presence of additional trap defects for the TNT series and a far higher defectivity for TNT0.5 compared to TNT0.1.

3.4. Photoluminescence

The photophysical properties of the samples were investigated by UV–vis fluorescence spectra, as reported in Fig. 3.

Two almost symmetrical curves are shown for each specimen, referring to the same electronic transitions, followed through excitation ("EX" spectra) or emission ("EM" spectra). The horizontal distance between the main symmetrical features quantifies the corresponding Stokes shifts. In excitation mode (Fig. 3b), the most intense band starts at roughly 2.9 eV and shows a broad maximum around 3.1–3.2 eV (395–397 nm), which corresponds to the adiabatic (vertical) transition across the anatase band gap. Owing to the indirect nature of this semiconductor, dissipative processes involving lattice phonons downshift the emission by ≈ 0.9–1.0 eV through non-radiative decay, resulting in a maximum close to 2.2 eV (Fig. 3a).

Three points are worth noting. First, all the spectra bear the same peak at ≈ 2.68 eV (461–464 nm), which undergoes an almost negligible Stokes shift of ≈ 0.017 eV. This feature is not attributable to N species, as it is already detectable in the pristine specimen T (Figure S4 in the Supporting Information).

Second, the signal of the TNN and TNU series closely resembles that of the blank reference (see Figure S4 in the Supporting Information), with root mean square deviations invariably lower than 0.025 (TNN) or 0.020 (TNU) normalized intensity units between the corresponding curves. Moreover, signals corresponding to 0.1 and 0.5 N/Ti nominal ratios are almost completely superimposable in both the TNN and TNU series, as it can be appreciated by visual inspection of Fig. 3. In other words, when the precursor is either urea or ammonia, the nominal N concentration does neither significantly affect the band edges, nor it is expected to strongly reduce the band gap. This agrees with the DRS results shown in Table 1 and Fig. 1.

The picture changes when the TNT series is considered (Fig. 3). A ≈0.11 eV large downshift of the maximum of the main absorption band is apparent at higher N concentration in the excitation scan mode. This is comparable with the decrease in the apparent band gap (0.1–0.2 eV) detected by DRS measurements (see Section 3.1). The shape of the high-energy excitation band is also influenced. As the shift does not affect the emission signal, we must conclude that non-radiative decay mechanisms reset the differences among distinct excitation paths, as the radiative step of the relaxation process starts from the energy of the absolute conduction band minimum (CBM) and results to a 2.1–2.2 eV wide step. On average, TNT spectra are significantly more different compared to the pristine reference, with root mean square deviations of ≈ 0.040 normalized intensity units. This further confirms that the electronic properties of TiO_2 are significantly affected only when the material comes from the triethylamine precursor, in accordance with DRS analyses (see Section 3.1).

3.5. Periodic DFT results

To clarify the relationship between defectivity and photophysical features, we exploited DFT to simulate an anatase TiO_2 supercell with a single V_O. Modeling of surface defect states was not attempted here as it requires a detailed knowledge of the crystallite morphology, while our

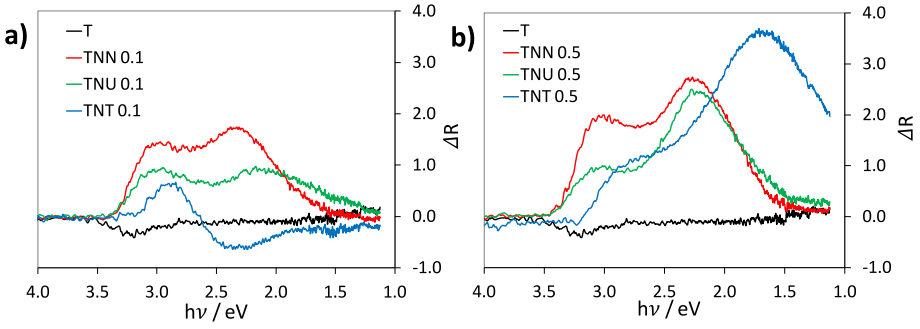

Fig. 2. Effect of UV irradiation, as variation in reflectance, on the optical properties of synthesized samples with N/Ti nominal ratio of 0.1 (a) and 0.5 (b). The relative spectrum of the pristine TiO_2 reference is reported for the sake of comparison.

Table 3
Least-squares fitting of differential DRS features reported in Fig. 2.

Sample	peak 1			peak 2			peak 3		
	position (eV)	width (eV)	area %	position (eV)	width (eV)	area %	position (eV)	width (eV)	area %
TNN0.1	3.00	0.39	30	2.32	0.67	70	–	–	–
TNN0.5	3.03	0.39	27	2.27	0.69	73	–	–	–
TNU0.1	2.97	0.45	36	2.10	0.75	64	–	–	–
TNU0.5	3.05	0.31	12	2.21	0.78	88	–	–	–
TNT0.1	2.88	0.30	35	2.30	0.49	44	1.51	0.64	21
TNT0.5	2.65	0.52	15	2.03	0.58	25	1.49	0.75	60

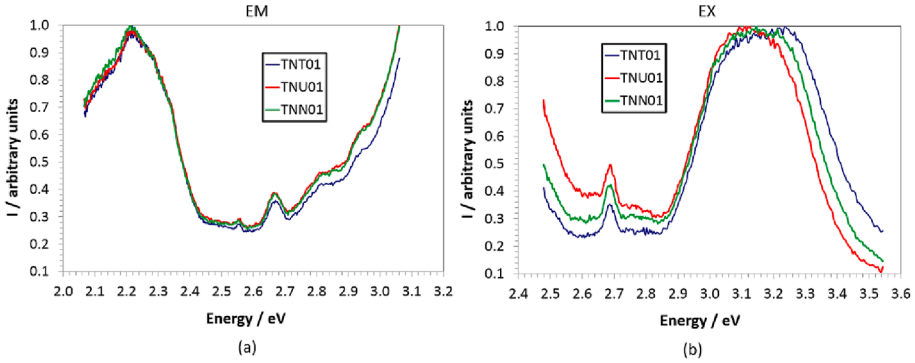

Fig. 3. Normalized [36] emission ("EM") (a) and excitation ("EX") UV–Vis fluorescence spectra for synthesized TiO_2 samples from different N sources (blue: triethylamine, red: urea, green: ammonia) with nominal N/Ti ratio of 0.1. Other concentrations are shown in Figure S4 in the Supporting Information . (For interpretation of the references to colour in this figure legend, the reader is referred to the web version of this article.)

samples are polymorph mixtures with a complex distribution of exposed facets. Furthermore, the modeling of surface vacancies was already addressed in the literature [60–61] showing that surface and subsurface states generate localized electronic states located below the conduction band of anatase TiO_2(1 0 1). For these reasons, our DFT calculations aim at modelling isolated bulk oxygen vacancies to disclose the genuine electronic and structural effects of V_O, getting rid of possible interactions with extrinsic dopants. [20,53] In particular, we look for the possible occurrence of colour centres and changes affecting the formal oxidation state of Ti ions. An oxygen vacancy implies that two excess electrons must be accounted for to ensure electroneutrality of the lattice. Within our PBE + U approach (U = 3.5 eV), among the possible stationary states we identified seven possible electronic states, differing in either the spin pairing or the relative localization of the excess electrons. A full description, as well as a discussion on the relative stability of the different states, is reported in Section S4. We consider the least stable nonmagnetic closed shell state as a suitable reference for the subsequent discussion. The six magnetic solutions all have lower energies. The magnetization yields to a total energy reduction with the most stable state presenting an energy −0.51 eV below the unpolarized case, implying a high localization of the excess electrons on different Ti atoms, one adjacent to the V_O and the other slightly further (Fig. 4a).

Two almost degenerate spin configurations are possible for this state, the one with parallel spins being more stable of the order of 10^{-3} eV. The –0.51 eV stabilization comes from the relief of unshielded Coulomb repulsion, which requires the excess electrons being localized into sites far apart from each other. At the same time, it is reasonable that electrons on different metal ions show a poor spin correlation in a diamagnetic matrix. Moreover, our ground-state simulations do not predict the formation of Farbe centres in the V_O void.

A closer insight can be achieved by inspecting the net charges of atoms involved in the internal reduction $Ti^{4+} + e^- \rightarrow Ti^{3+}$. We evaluated integral atomic charges from the topological analysis of the total charge density, according to the Bader's Quantum Theory of Atoms in Molecules (QTAIM); [62] full results are shown in Table S4-S5 in the Supporting Information . Granted that individual charges are not quantum observables, and henceforth any partitioning scheme is arbitrary to say the least, the QTAIM approach has the advantage of subdividing the total charge density into non-overlapping disjoint regions ("topological atoms", Ω's), whose boundaries are self-consistently set by the topology of the $\nabla\rho(\boldsymbol{r})$ vector field. Thus, the net charge of each topological atom is defined as:

$$q(\Omega) = Z_\Omega - e \bullet \int_\Omega \rho(r)dr \qquad (2)$$

where Z_Ω is the positive charge of the nucleus in Ω and e is the elementary charge. QTAIM charges $q(\Omega)$ depend on the electron population of the topological basin Ω, which can be taken as a reliable estimator of the oxidation state of that atom in its crystalline environment. [63–64] As for the present case, QTAIM charges confirm that the excess electrons are localized on specific Ti ions close to the V_O defect (Table S4 in the Supporting Information), which bear ≈ 15% more electrons than the corresponding bulk Ti atoms.

We note that the oxygen vacancy is equatorial with respect to both the reduced Ti centres (Fig. 4a). An analogous behaviour is observed for all the magnetic solutions (Table S4-S5 in the Supporting Information), with some V_O-neighbouring Ti atoms being reduced to some extent. Considering the band structure, the excess electrons inject new electronic states inside the band gap with respect to perfect TiO_2 (see Table S3 in the Supporting Information and Fig. 4b). It is clear from the above discussion that these must be localized on Ti centres close to the V_O, as it can be appreciated also from the projected density of state (PDOS) schemes (Figure S8 in the Supporting Information). Moreover, they fall deep inside the band gap, with a minimum distance from the conduction band minimum (CBM) of 0.9–1.0 eV for the two most stable solutions, as supported by a recent combined theoretical and experimental approach. [29] When related to the total DFT-predicted magnitude of the indirect band gap (2.48 eV), they correspond to ≈ 36–40% of the latter (Fig. 4b). Remarkably, this is in quantitative agreement with the UV–vis fluorescence results discussed in Section 3.4, where

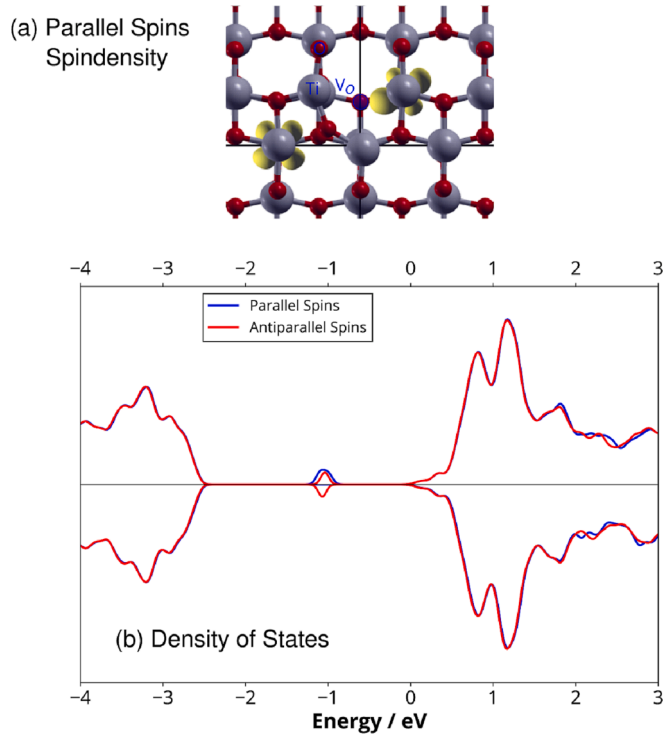

Fig. 4. a) spin density isolevel (yellow) at $5{\cdot}10^{-3}$ atomic units of the most stable state in oxygen–defective anatase TiO_2 with the PBE + U exchange and correlation potential. Ti atoms: grey. O atoms: red. The blue circle highlights the position of the oxygen vacancy. b) Density of States of defective anatase TiO_2 with the PBE + U exchange and correlation potential. Comparison of different magnetization states for the bulk and defective system. Upper and lower panels are for the two different unrestricted spin magnetization. (For interpretation of the references to colour in this figure legend, the reader is referred to the web version of this article.)

excitation and emission spectra show a signal at 1.06 eV from the indirect-gap CBM. Moreover, the highly localized nature of the defect complies well with the immaterial Stokes shift measured for the corresponding transition (see Section 3.4), indicating that the relaxation process is essentially radiative in nature. This is expected, considering that bulk V_O's can act as efficient recombination centres. Hence, bulk DFT calculations support an attribution of the spectral feature noted in UV–Vis fluorescence experiments at 2.68 eV to oxygen vacancies, in agreement with previous reports. [65].

3.6. Confocal microscopy

As the aforementioned transition falls in the blue region of the visible window (461–464 nm), confocal microscopy (CM) can be employed to quantify the relative amount of fluorescence attributable to emitting V_O centres in our samples. CM is an imaging technique that allows locating fluorophores with high spatial resolution (<0.5 μm), even in complex matrices. [66] In the present case, the specimen is a suspension of nanoparticle aggregates (Fig. 5), hence data processing was performed taking into account the issue of self-absorption (see Section 2.2).

In particular, I_D quantifies the average emitting density of regions whose fluorescence is not hampered by aggregation effects. Thus, I_D is uncorrelated with self-absorption (Figure S13 in the Supporting Information) and it can be taken as a least-biased intrinsic property of the material, genuinely related with the nature of V_O defects. Fig. 6 shows I_D estimates for the three series. Results are also summarized in Table S6 in the Supporting Information .

A first outcome from Fig. 6 is that TNT materials have the lowest fluorescence output: their I_D is almost halved with respect to T, despite of a similar self-absorption (Table S6 in the Supporting Information). This is quite surprising, as EXAFS results (Table 2) neatly demonstrate that the TNT series displays a promoted formation of extra oxygen vacancies. The latter can be attributed to an effective incorporation of extrinsic N defects in the lattice in the TNT series, according to Eq. 1. Furthermore, the trend shown in Fig. 6 countercorrelates with the expected amount of N that enters the lattice, as inferred from the distortion of the crystallographic unit cell of TiO_2 anatase (TNT > TNN > TNU) described elsewhere [7]. It should be noted that Fig. 6 compares the

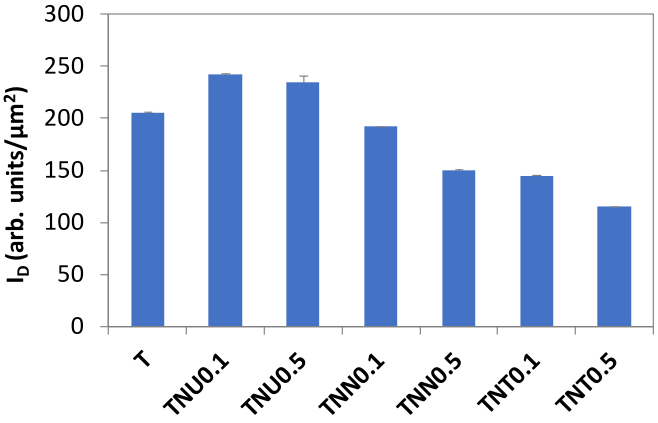

Fig. 6. Fluorescence density (in arbitrary units per μm^2) of the synthesized samples, as estimated by confocal microscopy.

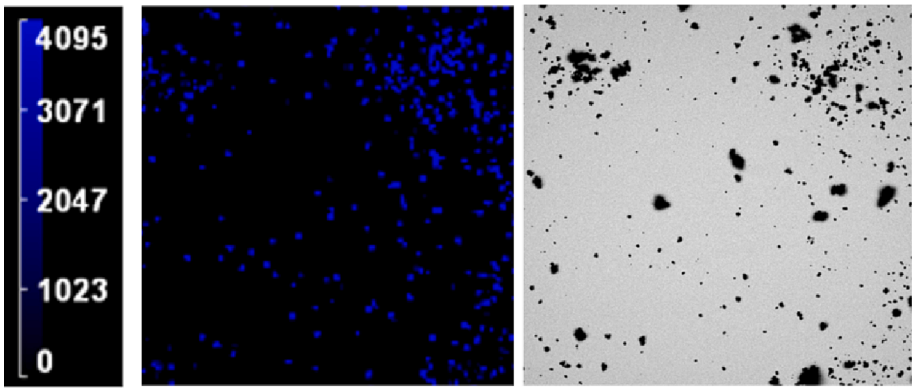

Fig. 5. Confocal images (40x, area: 310 × 310 μm^2, offset correction 50%, HV 700 V, laser intensity 10%) of TNN0.5. Left: fluorescence in false colors to enhance the fluorescence output. Legend in arbitrary units. Right: visible light. This picture has an illustrative purpose to see what information the confocal images convey; see Figures S10-12 to see all samples.

fluorescence emission from V_O centres, *i.e.* the amount of radiative recombination from these species, and not the actual density of oxygen vacancies. The discrepancy between EXAFS and CM outcomes entails that V_O centres with different de-excitation pathways exist in each series, as will be further discussed in Section 4.

3.7. Photocatalysis

The role played by these different defective ensembles on the photocatalytic performance of the material was investigated towards the degradation of a model volatile organic compound, ethanol, in the gas phase (Figures S14-S15). Ethanol was selected as model pollutant since its gas phase photocatalytic reaction mechanism has been investigated in detail. [67] Under UV light irradiation, pristine TiO_2 performs better than most of the visible-sensitized samples, both in terms of ethanol disappearance and of final mineralization (Table 1). This result could be rationalized considering the much lower specific surface area of N-modified samples with respect to the pristine reference. It is well-known that the morphological features of the photocatalyst play a major role on gas phase reactions: in the gas phase photocatalysis, only the adsorbed pollutant molecules can undergo redox reactions by photogenerated charge carriers or surface radicals. [67] Moreover, the occurrence of lattice defects has been related to poorer photocatalytic performance by promoting recombination [68] or lowering the oxidative potential of photogenerated charges. [31] Notably, the only exception is represented by TNN0.5, which showed promoted photocatalytic performance, despite the lower surface area. The enhanced performance could be possibly related to the higher anatase content and crystallinity.

The role of N-addition on the photocatalytic performance under visible light irradiation was also investigated. Overall, the reaction rates are much lower than under UV irradiation, as a result only the rate constant of ethanol degradation are here commented (Table 1). Interestingly, most of the visible-sensitized samples do not exhibit significantly enhanced performance compared to the pristine reference. The residual activity of the latter under visible irradiation is due to the light absorbance above 400 nm of anatase. The best performing samples belong to the TNT series, with the TNT0.1 showing a reaction rate under visible light one order of magnitude higher than that of pristine TiO_2. To compare the performance of the present best performing sample with literature benchmarks, the interested reader is referred to a recent review on the photocatalytic degradation of VOCs. [67].

4. Discussion

The reported experimental evidence underlines a diverse role of the three N sources in introducing intrinsic and extrinsic defects into the oxide lattice. Upon triethylamine addition in synthesis, the local structure and photophysical properties, in agreement with previous PXRD studies, [7] support N substitution of O atoms within the TiO_2 lattice, leading at high N nominal contents to a marked increase in the amount of V_O, in accordance with theoretical calculations. [69] Conversely, the TNN and TNU samples exhibit a localized visible-light absorption but miss the tell-tale signs of N substitutional doping (shift of the absorption edge and promotion of oxygen vacancies formation [69]), in accordance with previous reports of TiO_2 modification using either ammonia or urea. [31] However, the nature of visible-light inducing defects in these samples remains controversial. Promoted PL emission from the TNU series suggests a fast charge carrier recombination, possibly explaining the observed poor photocatalytic performance of these samples (Section 3.7). These observations also do not support the formation of efficient TiO_2/*g*-C_3N_4 heterojunctions in the present conditions, as also suggested by FTIR spectra (Section 3.1). Furthermore, the similar photophysical behaviour of TNN and TNU samples seems to underscore common traits related to trap sites (see e.g., photochromic and PL properties).

Samples from different N sources thus present notable differences in terms of V_O's density. CM results suggest that each series differs also in the de-excitation pathways available for V_O centres. Scheme 1 summarizes the mechanisms of photoexcitation and relaxation of defective TiO_2 here proposed on the grounds of the present spectroscopic analyses, theoretical calculations and literature results [20].

In this picture, V_O centres are responsible for a sharp transition at ≈2.7 eV, appreciable both in absorption and fluorescence spectra of all samples. The trend in the fluorescence emission of this transition mirrors, however, neither that in light absorption nor in the V_O content based on local structural data. It should be noted that our DFT calculations were performed assuming a bulk oxygen vacancy. It is worth noting that surface and subsurface vacancies could imply electronic transitions at lower energies [60–61] with respect to the characteristic 2.68 eV signature detected by photoluminescence measurements. The absence of fluorescence features related to surface-defects can be explained invoking the O_2-induced quenching of fluorescence. It is well known that, under the action of UV light, polycrystalline TiO_2 can promote the formation of highly reactive oxygen species (ROS), like superoxide radicals (O_2^-) [70] or singlet dioxygen ($^1O_2$). [71–72] Experimental evidence [70–71,73] suggests that ROS formation involves an initial absorption of ground-state triplet O_2 at surface V_O's, followed by an electron transfer from vacancy-related Ti^{3+} species. [74] The quenching of any characteristic emission of V_O's is likely a byproduct of the UV-induced interaction of surface vacancies with O_2. We hypothesize that the low I_D of TNT samples be ascribable to a higher concentration of surface V_O's. The combination of EXAFS and CM outcomes thus indicate that TNT materials have the greatest amount of surface V_O's compared to the pristine reference (Fig. 6). Conversely, V_O's are mainly of bulk nature in TNU, that is, they are buried deep inside the nanoparticles, being preserved from interaction with O_2. In this respect, it should be noted that TNU samples have lower surface area and porosity than the TNN and TNT series (Table 1). The TNN series exhibits an intermediate behaviour, with TNN0.1 showing a similar fluorescence emission than T, and TNN0.5 displaying a reduced PL emission, possibly related to the sample's higher crystallinity and promoted UV-light photocatalytic activity. This scenario awaits experimental confirmation through dedicated measurements in controlled oxidant environments. It is worth noting, however, that an analogue conclusion was drawn for O-defective CeO_2 nanoparticles, which were proposed to exploit quenching of fluorescence for applications in oxygen detection. [75].

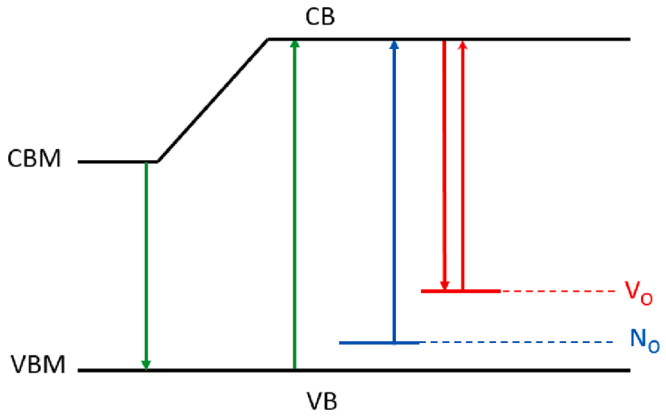

Scheme 1. Qualitative illustration of the main radiative excitation-relaxation processes in TiO_2-based nanoparticles discussed in this work. CBM and VBM are the conduction band minimum and the valence band maximum. Green: main absorption path, already active in bare anatase TiO_2. The difference in energy between CB and CBM corresponds to the Stokes shift seen in UV–vis fluorescence spectra and involves a phonon-mediated non-radiative decay. Blue: absorption from occupied shallow mid-gap states due to substitutional N (estimated from bulk plane-wave calculations [20]. Red: radiative excitation-relaxation process due to oxygen vacancies, with no significant Stokes shift (UV–vis fluorescence data, this work).

These diverse landscapes in terms of intrinsic and extrinsic defects give rise to notably different photochromic and photocatalytic properties. Transient absorption features have been related to trap states, hence have been used to investigate the defectivity of TiO_2. [11] Here, the photochromic peak at the highest energy falls at ca. 3.0 eV for the TNN and TNU series and < 3 eV for TNT samples, *i.e.* ca. 0.2 eV below the band gap value of each sample. Electron trapping states located ca. 0.26 eV below the CB edge have been previously related to Ti^{3+} ions. [11,76] Mendoza Diaz et al. recently studied the PL emission of TiO_2 samples using scavengers: a PL peak at ca. 2.9 eV was attributed to recombination between electrons trapped in shallow trapping states due to Ti^{3+} species associated with Ti interstitials, and holes in the VB. [29] With respect to PL transitions, here the transient absorption features are produced by UV irradiation over the course of minutes and are stable for several hours. Indeed, slow interconversions between electron traps, taking place over the course of minutes to hours at 0–50 °C, have been previously reported in reduced TiO_2 systems and attributed to equilibration in trap states involving changes in structure or stoichiometry. [77] Also the absorption feature centered between 2.2 and 2.3 eV has been previously reported and assigned to the $^2T_2$ to ^2E transition of Ti^{3+}. [78–79] Furthermore, Serpone and coauthors consistently reported a photochromic peak at 2.16 eV upon UV light irradiation of N-doped TiO_2 samples, which was attributed to Ti^{3+} centres [57,80] . The TNN and TNU photochromic features, as well as some of the TNT ones, could thus be related to photogenerated Ti^{3+} species. These features are observed only in the N-modified samples, suggesting that the addition of these external sources, particularly ammonia and urea, introduce electron donor species, which, in turn, lead to the formation of Ti^{3+} species upon light irradiation. [81].

Furthermore, the TNT0.5 sample shows a marked photochromic component at ca. 1.5 eV: this observation, along with the increased V_O content and low PL emission of this sample, suggests that this component could be related to Ti^{3+} species associated with surface V_O. Notably, Kuznetsov and coauthors [59] attributed a photochromic peak at 1.56 eV to extra-charged Ti^{3+} species ($Ti^{\delta+}$), such as two adjacent Ti^{3+} centers located near a single oxygen vacancy, whose formation occurs only at high density of photogenerated Ti^{3+} centers. Interestingly, the TNT sample displays optical features similar to black TiO_2 samples (red-shift of the absorption edge and extended visible light absorption), which have been attributed to the formation of high concentrations of Ti^{3+} in the surface disordered layer. [82].

A key issue is the stability of lattice defects. DRS spectra were acquired on both freshly prepared and aged samples (after 4 months of storage in the dark at room temperature). Ageing is appreciable by a change in the optical features specifically related to N-induced defects, such as electron donor centers and surface oxygen vacancies. Figure S16 in the Supporting Information reports the difference DRS spectra of N-modified samples, obtained by subtracting the spectrum of the freshly prepared sample from that of the aged one. Interestingly, the difference spectra show a loss of visible light absorption in time, with the same features characteristic of N-modification in photochromic experiments (compare with Fig. 2). Therefore, these results suggest that N-related species are unstable, in agreement with previous reports. [83] In particular, the feature at 1.5 eV in TNT spectra, which was related to Ti^{3+} associated with surface oxygen vacancies, shows an abrupt decrease in time.

Hence, the photochromic behaviour of all N modified samples highlights the occurrence of trap states for photogenerated electrons due to lattice defects formed upon N addition during synthesis. Overall, the presence of trap sites in N-modified samples goes hand in hand with poorer photocatalytic performance under UV irradiation. The only notable exception is TNN0.5: This sample is characterized by larger crystallites and higher anatase content, which have been related to reduced recombination of photogenerated charges (see confocal microscopy results) and promoted photocatalytic activity.

Visible-light tests also show mixed results. The visible-absorbing species in TNU and TNN fail to promote visible-light activity, which could be related to an insufficient oxidation potential or mobility of trapped holes to generate highly oxidizing radicals. [31,84] Conversely, the TNT series displays visible light activity, which could be due to its N substitutional doping. In the TNT series, the highest activity is achieved by TNT0.1. Notably, TNT0.1 is the only sample displaying some detrapping effects upon light irradiation. It is widely accepted that charge transfer occurs from Ti^{3+} states to singly occupied N-states: [85]

$$Ti^{3+} + N_b^{\cdot} \rightleftharpoons Ti^{4+} + N_b^{-} \quad (2)$$

Moreover, light irradiation regenerates paramagnetic $N_b^{\cdot}$ centers from N_b^{-} states by exciting electrons to the conduction band, which are then captured by adsorbed O_2. [85] Hence, the presence of substitutional nitrogen could promote detrapping of Ti^{3+}-related states. However, if V_O's are in excess compared to N states, the Ti^{3+} states still remain partially populated. [20] This could explain why the V_O-rich TNT0.5 sample displays such a different photochromic behavior compared to TNT0.1. The presence of trap sites related to extra-charged Ti^{3+} could, in turn, rationalize the lower visible-light activity of TNT0.5 compared to TNT0.1.

5. Conclusions

In this work, we applied a multidisciplinary approach, including advanced spectroscopy and microscopy methods, to investigate the role of oxygen vacancies (V_O's) in highly defective nanostructured TiO_2 matrices. Plane wave bulk quantum simulations complemented the experimental picture. The purpose was twofold: on the one hand, to explore the distribution and role of surface and bulk V_O's; on the other hand, to study how V_O's may affect the photophysical and photochemical properties of TiO_2. The amount of V_O species was tuned by addition of an extrinsic defect, nitrogen. As a matter of fact, thermodynamics ensures that the concentration of bulk N and extra V_O's are correlated, despite being both not easily amenable to quantitative experimental determination.

UV–vis fluorescence showed a characteristic spectral signal in the blue range of the visible window (≈ 2.7 eV, 461–464 nm), which was present already in the pristine TiO_2 reference. High-grade DFT simulations demonstrated that this signature is specific of bulk V_O defects. Excess electrons coming from a V_O are highly localized on at least two reduced Ti ions around the vacancy. In turn, this produces sharp mid-gap states, which are involved in rapid excitation-recombination processes with almost no Stokes shift.

Further insights into the quantity and distribution of V_O's within the nanostructured particles were obtained by comparing local structural information, gained by a combination of EXAFS and DFT data, with fluorescence density output per μm^2, measured by confocal microscopy. We hypothesize that, in the case of the TNT series, the V_O excess does not promote fluorescence emission due to the surface nature of these defects, which can interact with adsorbed oxygen species under UV pumping. We propose that confocal microscopy combined with local structural information might be employed as a tool to discriminate the distribution of V_O's in nanostructured TiO_2.

Actually, a lowered fluorescence in N-modified species is correlated with a promoted photocatalytic activity, as TNN0.5 and the TNT series are the best performing samples under UV and visible sources, respectively. The photocatalytic features of the latter samples could be attributed to substitutional N doping, as other N-related defects, such as those prevalent in the TNU and TNN series, are not visible-active despite absorbing visible-light.

The intrinsic defects play a notable role as well in the photochromic and photocatalytic properties of the N-modified samples. A good balance between the extrinsic and intrinsic defects, such as in TNT0.1, seems related to detrapping phenomena and an ensuing enhanced photocatalytic activity in the visible region. A further increase in V_O

content (even surface ones) could promote the formation of other electron traps, such as photo-induced extra-charged Ti^{3+} species, slightly worsening the photocatalytic performance.

CRediT authorship contribution statement

Daniela Meroni: Writing – review & editing, Validation, Formal analysis. **Carolina Cionti:** Methodology, Formal analysis. **Lucia Silvestrini:** Methodology, Investigation, Formal analysis. **Noga Gal:** Methodology, Investigation, Formal analysis. **Marco Cazzaniga:** Investigation, Formal analysis, Data curation. **Michele Ceotto:** Investigation, Formal analysis, Data curation. **Giacomo Buccella:** Investigation, Formal analysis, Data curation. **Leonardo Lo Presti:** Writing – original draft, Supervision, Methodology, Formal analysis, Conceptualization. **Giuseppe Cappelletti:** Writing – review & editing, Project administration, Conceptualization.

Declaration of Competing Interest

The authors declare that they have no known competing financial interests or personal relationships that could have appeared to influence the work reported in this paper.

Data availability

Data will be made available on request.

Appendix A. Supplementary data

Supplementary data to this article can be found online at https://doi.org/10.1016/j.jphotochem.2023.114916.

References

[1] R. Gusain, K. Gupta, P. Joshi, O.P. Khatri, Adsorptive removal and photocatalytic degradation of organic pollutants using metal oxides and their composites: A comprehensive review, Adv Colloid Interface Sci. 272 (2019), 102009, https://doi.org/10.1016/j.cis.2019.102009.

[2] J. Shi, J. Zhang, L. Yang, M. Qu, D. Qi, K.H.L. Zhang, Wide Bandgap Oxide Semiconductors: from Materials Physics to Optoelectronic Devices, Adv. Mater. 33 (2021) 2006230, https://doi.org/10.1002/adma.202006230.

[3] H. Ji, W. Zeng, Y. Li, Gas sensing mechanisms of metal oxide semiconductors: a focus review, Nanoscale 11 (2019) 22664–22684, https://doi.org/10.1039/C9NR07699A.

[4] T. Zhang, Q. He, J. Yu, A. Chen, Z. Zhang, J. Pan, Recent progress in improving strategies of inorganic electron transport layers for perovskite solar cells, Nano Energy 104 (2022), 107918, https://doi.org/10.1016/J.NANOEN.2022.107918.

[5] J. Liu, Z. Luo, X. Mao, Y. Dong, L. Peng, D. Sun-Waterhouse, J.V. Kennedy, G.I. N. Waterhouse, J. Liu, Z. Luo, X. Mao, Y. Dong, L. Peng, D. Sun-Waterhouse, G.I. N. Waterhouse, J.V. Kennedy, Recent Advances in Self-Supported Semiconductor Heterojunction Nanoarrays as Efficient Photoanodes for Photoelectrochemical Water Splitting, Small 18 (2022) 2204553, https://doi.org/10.1002/SMLL.202204553.

[6] L.K. Putri, B.J. Ng, W.J. Ong, S.P. Chai, A.R. Mohamed, Toward Excellence in Photocathode Engineering for Photoelectrochemical CO2 Reduction: Design Rationales and Current Progress, Adv Energy Mater. 12 (2022) 2201093, https://doi.org/10.1002/AENM.202201093.

[7] L. Lo Presti, M. Ceotto, F. Spadavecchia, G. Cappelletti, D. Meroni, R.G. Acres, S. Ardizzone, Role of the Nitrogen Source in Determining Structure and Morphology of N-Doped Nanocrystalline TiO 2, J. Phys. Chem. C 118 (2014) 4797–4807, https://doi.org/10.1021/jp412394e.

[8] F. Spadavecchia, G. Cappelletti, S. Ardizzone, M. Ceotto, M.S. Azzola, L. Lo Presti, G. Cerrato, L. Falciola, Role of Pr on the Semiconductor Properties of Nanotitania. An Experimental and First-Principles Investigation, J. Phys. Chem. C 116 (2012) 23083–23093, https://doi.org/10.1021/jp307303n.

[9] C. Marchiori, G. Di Liberto, G. Soliveri, L. Loconte, L. Lo Presti, D. Meroni, M. Ceotto, C. Oliva, S. Cappelli, G. Cappelletti, C. Aieta, S. Ardizzone, Unraveling the Cooperative Mechanism of Visible-Light Absorption in Bulk N,Nb Codoped TiO_2 Powders of Nanomaterials, The Journal of Physical Chemistry C. 118 (n.d.) 24152–24164. https://doi.org/10.1021/jp507143z.

[10] L. Rimoldi, C. Ambrosi, G. Di Liberto, L. Lo Presti, M. Ceotto, C. Oliva, D. Meroni, S. Cappelli, G. Cappelletti, G. Soliveri, G. Soliveri, S. Ardizzone, Impregnation versus Bulk Synthesis: How the Synthetic Route Affects the Photocatalytic Efficiency of Nb/Ta: N Codoped TiO<inf>2</inf> Nanomaterials, J. Phys. Chem. C 119 (2015) 24104–24115, https://doi.org/10.1021/acs.jpcc.5b06827.

[11] B. Liu, X. Zhao, J. Yu, I.P. Parkin, A. Fujishima, K. Nakata, Intrinsic intermediate gap states of TiO2 materials and their roles in charge carrier kinetics, J Photochem Photobiol C: Photochem Rev 39 (2019) 1–57, https://doi.org/10.1016/J.JPHOTOCHEMREV.2019.02.001.

[12] S. Bai, N. Zhang, C. Gao, Y. Xiong, Defect engineering in photocatalytic materials, Nano Energy 53 (2018) 296–336, https://doi.org/10.1016/J.NANOEN.2018.08.058.

[13] J. Nowotny, M.A. Alim, T. Bak, M.A. Idris, M. Ionescu, K. Prince, M.Z. Sahdan, K. Sopian, M.A. Mat Teridi, W. Sigmund, Defect chemistry and defect engineering of TiO2-based semiconductors for solar energy conversion, Chem Soc Rev. 44 (2015) 8424–8442, https://doi.org/10.1039/C4CS00469H.

[14] L. Hou, Z. Guan, M. Zhang, C. He, Q. Li, J. Yang, Adjusting the ratio of bulk single-electron-trapped oxygen vacancies/surface oxygen vacancies in TiO2 for efficient photocatalytic hydrogen evolution, Catal, Sci Technol. 8 (2018) 2809–2817, https://doi.org/10.1039/C8CY00644J.

[15] X. Yu, B. Kim, Y.K. Kim, Highly enhanced photoactivity of anatase TiO2 nanocrystals by controlled hydrogenation-induced surface defects, ACS Catal. 3 (2013) 2479–2486, https://doi.org/https://doi.org/10.1021/cs4005776.

[16] Q. Sun, D. Cortie, S. Zhang, T.J. Frankcombe, G. She, J. Gao, L.R. Sheppard, W. Hu, H. Chen, S. Zhuo, D. Chen, R.L. Withers, G. McIntyre, D. Yu, W. Shi, Y. Liu, The Formation of Defect-Pairs for Highly Efficient Visible-Light Catalysts, Adv Mater. 29 (2017) 3601, https://doi.org/10.1002/adma.201605123.

[17] Q. Wu, Q. Zheng, R. Van De Krol, Creating oxygen vacancies as a novel strategy to form tetrahedrally coordinated Ti 4+ in Fe/TiO 2 nanoparticles, J. Phys. Chem. C 116 (2012) 7219–7226, https://doi.org/https://doi.org/10.1021/jp212577g.

[18] D. Ariyanti, L. Mills, J. Dong, Y. Yao, W. Gao, NaBH4 modified TiO2: Defect site enhancement related to its photocatalytic activity, Mater Chem Phys. 199 (2017) 571–576, https://doi.org/10.1016/J.MATCHEMPHYS.2017.07.054.

[19] C. Di Valentin, G. Pacchioni, A. Selloni, Reduced and n-type doped TiO2: Nature of Ti3+ species, J. Phys. Chem. C 113 (2009) 20543–20552, https://doi.org/https://doi.org/10.1021/jp9061797.

[20] F. Spadavecchia, G. Cappelletti, S. Ardizzone, M. Ceotto, L. Falciola, Electronic structure of pure and N-doped TiO2 nanocrystals by electrochemical experiments and first principles calculations, J. Phys. Chem. C 115 (2011) 6381–6391, https://doi.org/10.1021/jp2003968.

[21] B. chu, X. Ou, L. Wei, H. Liu, K. chen, Q. Qin, L. Meng, M. Fan, B. Li, L. Dong, Insight into the effect of oxygen vacancies and OH groups on anatase TiO2 for CO oxidation: A combined FT-IR and density functional theory study, Molecular Catalysis. 511 (2021) 111755. https://doi.org/10.1016/J.MCAT.2021.111755.

[22] Q. Sun, D. Cortie, S. Zhang, T.J. Frankcombe, G. She, J. Gao, L.R. Sheppard, W. Hu, H. Chen, S. Zhuo, D. Chen, R.L. Withers, G. McIntyre, D. Yu, W. Shi, Y. Liu, The Formation of Defect-Pairs for Highly Efficient Visible-Light Catalysts, Adv. Mater. 29 (2017) 1–6, https://doi.org/10.1002/adma.201605123.

[23] M. Kobielusz, A. Nitta, W. MacYk, B. Ohtani, Combined Spectroscopic Methods of Determination of Density of Electronic States: Comparative Analysis of Diffuse Reflectance Spectroelectrochemistry and Reversed Double-Beam Photoacoustic Spectroscopy, J. Phys. Chem. Lett. 12 (2021) 3019–3025, https://doi.org/10.1021/ACS.JPCLETT.1C00262/ASSET/IMAGES/LARGE/JZ1C00262_0004.JPEG.

[24] M. Keulemans, S.W. Verbruggen, B. Hauchecorne, J.A. Martens, S. Lenaerts, Activity versus selectivity in photocatalysis: Morphological or electronic properties tipping the scale, J Catal. 344 (2016) 221–228, https://doi.org/10.1016/J.JCAT.2016.09.033.

[25] S. Ikeda, N. Sugiyama, S.Y. Murakami, H. Kominami, Y. Kera, H. Noguchi, K. Uosaki, T. Torimoto, B. Ohtani, Quantitative analysis of defective sites in titanium(IV) oxide photocatalyst powders, PCCP 5 (2003) 778–783, https://doi.org/10.1039/B206594K.

[26] G. Li, R. Huang, C. Zhu, G. Jia, S. Zhang, Q. Zhong, Effect of oxygen vacancies and its quantity on photocatalytic oxidation performance of titanium dioxide for NO removal, Colloids Surf A Physicochem Eng Asp. 614 (2021), 126156, https://doi.org/10.1016/J.COLSURFA.2021.126156.

[27] T. Cao, T. Xia, L. Zhou, G. Li, X. Chen, H. Tian, J. Zhao, J.O. Wang, W. Zhang, S. Li, S. Meng, H. Guo, Distribution and concentration of surface oxygen vacancy of TiO2 and its photocatalytic activity, J Phys D Appl Phys. 53 (2020), 424001, https://doi.org/10.1088/1361-6463/AB9D99.

[28] J. Huang, L. Dou, J. Li, J. Zhong, M. Li, T. Wang, Excellent visible light responsive photocatalytic behavior of N-doped TiO2 toward decontamination of organic pollutants, J Hazard Mater. 403 (2021), 123857, https://doi.org/10.1016/J.JHAZMAT.2020.123857.

[29] M.I. Mendoza Diaz, A. Balocchi, K. Oyekan, K. Tan, W.G. Vandenberghe, A. Esteve, C. Rossi, Dominant role of OH− and Ti3+ defects on the electronic structure of TiO2 thin films for water splitting, Dalton Trans. 51 (2022) 15300–15311, https://doi.org/10.1039/D2DT01871C.

[30] M. Ceotto, L. Lo Presti, G. Cappelletti, D. Meroni, F. Spadavecchia, R. Zecca, M. Leoni, P. Scardi, C.L. Bianchi, S. Ardizzone, About the Nitrogen Location in Nanocrystalline N-Doped TiO2: Combined DFT and EXAFS Approach, J. Phys. Chem. C 116 (2012) 1764–1771, https://doi.org/10.1021/jp2097636.

[31] J.A. Rengifo-Herrera, P. Osorio-Vargas, C. Pulgarin, A critical review on N-modified TiO2 limits to treat chemical and biological contaminants in water, Evidence that enhanced visible light absorption does not lead to higher degradation rates under whole solar light, J Hazard Mater. 425 (2022), 127979, https://doi.org/10.1016/J.JHAZMAT.2021.127979.

[32] D. Mitoraj, H. Kisch, The Nature of Nitrogen-Modified Titanium Dioxide Photocatalysts Active in Visible Light, Angew. Chem. Int. Ed. 47 (2008) 9975–9978, https://doi.org/10.1002/ANIE.200800304.

[33] L. Rimoldi, A. Giordana, G. Cerrato, E. Falletta, D. Meroni, Insights on the photocatalytic degradation processes supported by TiO2/WO3 systems, The case of ethanol and tetracycline, Catal Today. 328 (2019) 210–215, https://doi.org/10.1016/J.CATTOD.2018.11.035.
[34] B. Ravel, M. Newville, Athena, artemis, hephaestus,, data analysis for X-ray absorption spectroscopy using IFEFFIT, Urn:Issn:0909–0495. 12 (2005) 537–541, https://doi.org/10.1107/S0909049505012719.
[35] M. Newville, IFEFFIT: Interactive XAFS analysis and FEFF fitting, J Synchrotron Radiat. 8 (2001) 322–324, https://doi.org/10.1107/S0909049500016964.
[36] G. Angulo, G. Grampp, A. Rosspeintner, Recalling the appropriate representation of electronic spectra, Spectrochim Acta A Mol Biomol Spectrosc. 65 (2006) 727–731, https://doi.org/10.1016/J.SAA.2006.01.007.
[37] J. Schindelin, I. Arganda-Carreras, E. Frise, V. Kaynig, M. Longair, T. Pietzsch, S. Preibisch, C. Rueden, S. Saalfeld, B. Schmid, J.Y. Tinevez, D.J. White, V. Hartenstein, K. Eliceiri, P. Tomancak, A. Cardona, Fiji: an open-source platform for biological-image analysis, Nature Methods 2012 9:7. 9 (2012) 676–682. https://doi.org/10.1038/nmeth.2019.
[38] G. Soliveri, S. Ardizzone, A. Antonello, D. Meroni, G. Cappelletti, Photocatalytic remediation of indoor pollution by transparent TiO2 films, Catal Today. 230 (2014) 35–40, https://doi.org/10.1016/j.cattod.2013.12.033.
[39] P. Giannozzi, O. Andreussi, T. Brumme, O. Bunau, M. Buongiorno Nardelli, M. Calandra, R. Car, C. Cavazzoni, D. Ceresoli, M. Cococcioni, N. Colonna, I. Carnimeo, A. Dal Corso, S. De Gironcoli, P. Delugas, R.A. Distasio, A. Ferretti, A. Floris, G. Fratesi, G. Fugallo, R. Gebauer, U. Gerstmann, F. Giustino, T. Gorni, J. Jia, M. Kawamura, H.Y. Ko, A. Kokalj, E. Küçükbenli, M. Lazzeri, M. Marsili, N. Marzari, F. Mauri, N.L. Nguyen, H.V. Nguyen, A. Otero-De-La-Roza, L. Paulatto, S. Poncé, D. Rocca, R. Sabatini, B. Santra, M. Schlipf, A.P. Seitsonen, A. Smogunov, I. Timrov, T. Thonhauser, P. Umari, N. Vast, X. Wu, S. Baroni, Advanced capabilities for materials modelling with Quantum ESPRESSO, J. Phys. Condens. Matter 29 (2017), 465901, https://doi.org/10.1088/1361-648X/AA8F79.
[40] P. Giannozzi, S. Baroni, N. Bonini, M. Calandra, R. Car, C. Cavazzoni, D. Ceresoli, G.L. Chiarotti, M. Cococcioni, I. Dabo, A. Dal Corso, S. De Gironcoli, S. Fabris, G. Fratesi, R. Gebauer, U. Gerstmann, C. Gougoussis, A. Kokalj, M. Lazzeri, L. Martin-Samos, N. Marzari, F. Mauri, R. Mazzarello, S. Paolini, A. Pasquarello, L. Paulatto, C. Sbraccia, S. Scandolo, G. Sclauzero, A.P. Seitsonen, A. Smogunov, P. Umari, R.M. Wentzcovitch, QUANTUM ESPRESSO: a modular and open-source software project for quantum simulations of materials, J. Phys. Condens. Matter 21 (2009), 395502, https://doi.org/10.1088/0953-8984/21/39/395502.
[41] P. Giannozzi, O. Baseggio, P. Bonfà, D. Brunato, R. Car, I. Carnimeo, C. Cavazzoni, S. De Gironcoli, P. Delugas, F. Ferrari Ruffino, A. Ferretti, N. Marzari, I. Timrov, A. Urru, S. Baroni, Quantum ESPRESSO toward the exascale, J Chem Phys. 152 (2020), 154105, https://doi.org/10.1063/5.0005082.
[42] Z. Hu, H. Metiu, Choice of U for DFT+ U calculations for titanium oxides, J. Phys. Chem. C 115 (2011) 5841–5845, https://doi.org/https://doi.org/10.1021/jp111350u.
[43] M.E. Arroyo-De Dompablo, A. Morales-Garca, M. Taravillo, DFT+U calculations of crystal lattice, electronic structure, and phase stability under pressure of TiO2 polymorphs, J Chem Phys. 135 (2011), 054503, https://doi.org/10.1063/1.3617244.
[44] U. Diebold, The surface science of titanium dioxide, Surf Sci Rep. 48 (2003) 53–229, https://doi.org/10.1016/S0167-5729(02)00100-0.
[45] G. Mattioli, F. Filippone, P. Alippi, A. Amore Bonapasta, Ab initio study of the electronic states induced by oxygen vacancies in rutile and anatase TiO2, Phys Rev B Condens Matter Mater Phys. 78 (2008) 3–6, https://doi.org/10.1103/PhysRevB.78.241201.
[46] E. Finazzi, C. Di Valentin, G. Pacchioni, A. Selloni, Excess electron states in reduced bulk anatase TiO2: Comparison of standard GGA, GGA+U, and hybrid DFT calculations, J Chem Phys. 129 (2008), 154113, https://doi.org/10.1063/1.2996362.
[47] B.J. Morgan, G.W. Watson, Intrinsic n-type defect formation in TiO2: A comparison of rutile and anatase from GGA+U calculations, J. Phys. Chem. C 114 (2010) 2321–2328, https://doi.org/https://doi.org/10.1021/jp9088047.
[48] K. Yang, Y. Dai, B. Huang, Y.P. Feng, Density-functional characterization of antiferromagnetism in oxygen-deficient anatase and rutile TiO2, Phys Rev B Condens Matter Mater Phys. 81 (2010), 033202 https://doi.org/https://doi.org/10.1103/PhysRevB.81.033202.
[49] T. Yamamoto, T. Ohno, A hybrid density functional study on the electron and hole trap states in anatase titanium dioxide, PCCP 14 (2011) 589–598, https://doi.org/10.1039/C1CP21547G.
[50] A. Raghav, A. Tri Hanindriyo, K. Utimula, M. Abbasnejad, R. Maezono, E. Panda, Intrinsic electronic defect states of anatase using density functional theory, Comput Mater Sci. 184 (2020), 109925, https://doi.org/10.1016/J.COMMATSCI.2020.109925.
[51] A. Otero-de-la-Roza, M.A. Blanco, A.M. Pendás, V. Luaña, Critic: a new program for the topological analysis of solid-state electron densities, Comput Phys Commun. 180 (2009) 157–166, https://doi.org/10.1016/J.CPC.2008.07.018.
[52] A. Otero-De-La-Roza, E.R. Johnson, V. Luaña, Critic2: A program for real-space analysis of quantum chemical interactions in solids, Comput Phys Commun. 185 (2014) 1007–1018, https://doi.org/10.1016/J.CPC.2013.10.026.
[53] D. Meroni, S. Ardizzone, G. Cappelletti, C. Oliva, M. Ceotto, D. Poelman, H. Poelman, Photocatalytic removal of ethanol and acetaldehyde by N-promoted TiO 2 films: The role of the different nitrogen sources, Catal Today. 161 (2011) 169–174, https://doi.org/10.1016/j.cattod.2010.08.013.
[54] N. Boonprakob, N. Wetchakun, S. Phanichphant, D. Waxler, P. Sherrell, A. Nattestad, J. Chen, B. Inceesungvorn, Enhanced visible-light photocatalytic activity of g-C3N4/TiO2 films, J Colloid Interface Sci. 417 (2014) 402–409, https://doi.org/10.1016/J.JCIS.2013.11.072.
[55] M. Ceotto, L. Lo Presti, G. Cappelletti, D. Meroni, F. Spadavecchia, R. Zecca, M. Leoni, P. Scardi, C.L. Bianchi, S. Ardizzone, About the nitrogen location in nanocrystalline N-doped TiO <inf>2</inf>: Combined DFT and EXAFS approach, J. Phys. Chem. C 116 (2012) 1764–1771, https://doi.org/10.1021/jp2097636.
[56] F. Howard, C J, Sabine, T M, Dickson, Structural and Thermal Parameters for Rutile and Anatase, Acta Crystallographica B. 47 (1991) 462–468.
[57] V.N. Kuznetsov, N.I. Glazkova, R.V. Mikhaylov, N. Serpone, In situ study of photo- and thermo-induced color centers in photochromic rutile TiO2 in the temperature range 90–720 K, Photochem. Photobiol. Sci. 15 (2016) 1289–1298, https://doi.org/10.1039/C6PP00163G.
[58] V.N. Kuznetsov, N.I. Glazkova, R.V. Mikhaylov, N. Serpone, Additional Specific Channel of Photoactivation of Solid Semiconductors. A Revisit of the Thermo-/Photo-Stimulated Bleaching of Photoinduced Ti3+ Color Centers in Visible-Light-Active Photochromic Rutile Titania, J. Phys. Chem. C 122 (2018) 13294–13303, https://doi.org/https://doi.org/10.1021/acs.jpcc.7b08998.
[59] V.N. Kuznetsov, N.I. Glazkova, R.V. Mikhaylov, A.V. Kozhevina, N. Serpone, Photophysics of color centers in visible-light-active rutile titania, Evidence of the photoformation and trapping of charge carriers from advanced diffuse reflectance spectroscopy and mass spectrometry, Catal Today. 340 (2020) 58–69, https://doi.org/10.1016/J.CATTOD.2018.09.022.
[60] M.A. Ha, A.N. Alexandrova, Oxygen Vacancies of Anatase(101): Extreme Sensitivity to the Density Functional Theory Method, J Chem Theory Comput. 12 (2016) 2889–2895, https://doi.org/10.1021/ACS.JCTC.6B00095/ASSET/IMAGES/LARGE/CT-2016-00095V_0006.JPEG.
[61] N.S. Portillo-Vélez, O. Olvera-Neria, I. Hernández-Pérez, A. Rubio-Ponce, Localized electronic states induced by oxygen vacancies on anatase TiO2 (101) surface, Surf Sci. 616 (2013) 115–119, https://doi.org/10.1016/J.SUSC.2013.06.006.
[62] R.F.W. Bader, Atoms in molecules. A quantum theory, 1st ed.,, Oxford University Press, Oxford U.K, 1995.
[63] L. Lo Presti, V. Pifferi, G. Di Liberto, G. Cappelletti, L. Falciola, G. Cerrato, M. Ceotto, Direct measurement and modeling of spontaneous charge migration across anatase–brookite nanoheterojunctions, J Mater Chem A Mater. 9 (2021) 7782–7790, https://doi.org/10.1039/D1TA01040A.
[64] G. Di Liberto, V. Pifferi, L. Lo Presti, M. Ceotto, L. Falciola, Atomistic Explanation for Interlayer Charge Transfer in Metal-Semiconductor Nanocomposites: The Case of Silver and Anatase, J. Phys. Chem. Lett. 8 (2017) 5372–5377, https://doi.org/10.1021/acs.jpclett.7b02555.
[65] Y. Lei, L.D. Zhang, G.W. Meng, G.H. Li, X.Y. Zhang, C.H. Liang, W. Chen, S. X. Wang, Preparation and photoluminescence of highly ordered TiO2 nanowire arrays, Appl Phys Lett. 78 (2001) 1125, https://doi.org/10.1063/1.1350959.
[66] S.W. Paddock, Confocal Microscopy. Methods and Protocols, 2nd ed., Springer New York, New York, NY, 2014. https://doi.org/10.1007/978-1-60761-847-8.
[67] E. Pargoletti, L. Rimoldi, D. Meroni, G. Cappelletti, Photocatalytic removal of gaseous ethanol, acetaldehyde and acetic acid: from a fundamental approach to real cases, Https://Doi.Org/10.1080/09506608.2021.2017390. 67 (2022) 864–897, https://doi.org/10.1080/09506608.2021.2017390.
[68] J. Tang, A.J. Cowan, J.R. Durrant, D.R. Klug, Mechanism of O2 production from water splitting: Nature of charge carriers in nitrogen doped nanocrystalline TiO2 films and factors limiting O2 production, J. Phys. Chem. C 115 (2011) 3143–3150, https://doi.org/https://doi.org/10.1021/jp1080093.
[69] C. Di Valentin, G. Pacchioni, A. Selloni, S. Livraghi, E. Giamello, Characterization of paramagnetic species in N-doped TiO 2 powders by EPR spectroscopy and DFT calculations, J. Phys. Chem. B 109 (2005) 11414–11419, https://doi.org/https://doi.org/10.1021/jp051756t.
[70] E. Carter, A.F. Carley, D.M. Murphy, Evidence for O2- radical stabilization at surface oxygen vacancies on polycrystalline TiO2, J. Phys. Chem. C 111 (2007) 10630–10638, https://doi.org/https://doi.org/10.1021/jp0729516.
[71] A. Jańczyk, E. Krakowska, G. Stochel, W. Macyk, Singlet oxygen photogeneration at surface modified titanium dioxide, J Am Chem Soc. 128 (2006) 15574–15575, https://doi.org/https://doi.org/10.1021/ja065970m.
[72] M. Chiesa, S. Livraghi, M.C. Paganini, E. Salvadori, E. Giamello, Nitrogen-doped semiconducting oxides, Implications on photochemical, photocatalytic and electronic properties derived from EPR spectroscopy, Chem Sci. 11 (2020) 6623–6641, https://doi.org/10.1039/D0SC02876B.
[73] D.C. Hurum, A.G. Agrios, K.A. Gray, T. Rajh, M.C. Thurnauer, Explaining the enhanced photocatalytic activity of Degussa P25 mixed-phase TiO2 using EPR, J. Phys. Chem. B 107 (2003) 4545–4549, https://doi.org/https://doi.org/10.1021/jp0273934.
[74] C. Murata, H. Yoshida, J. Kumagai, T. Hattori, Active sites and active oxygen species for photocatalytic epoxidation of propene by molecular oxygen over TiO2-SiO2 binary oxides, J. Phys. Chem. B 107 (2003) 4364–4373, https://doi.org/https://doi.org/10.1021/jp0277006.
[75] N. Shehata, K. Meehan, D.E. Leber, Fluorescence quenching in ceria nanoparticles: dissolved oxygen molecular probe with relatively temperature insensitive Stern-Volmer constant up to 50°C 6 (2012) 063529, https://doi.org/10.1117/1.JNP.6.063529.
[76] P. Reckers, M. Dimamay, J. Klett, S. Trost, K. Zilberberg, T. Riedl, B.A. Parkinson, J. Brötz, W. Jaegermann, T. Mayer, Deep and shallow TiO2 gap states on cleaved anatase single crystal (101) surfaces, nanocrystalline anatase films, and ALD titania ante and post annealing, J. Phys. Chem. C 119 (2015) 9890–9898, https://doi.org/https://doi.org/10.1021/acs.jpcc.5b01264.
[77] J.L. Peper, D.J. Vinyard, G.W. Brudvig, J.M. Mayer, Slow Equilibration between Spectroscopically Distinct Trap States in Reduced TiO2 Nanoparticles, J Am Chem

Soc. 139 (2017) 2868–2871, https://doi.org/https://doi.org/10.1021/jacs.6b12112.
[78] T. Sekiya, K. Ichimura, M. Igarashi, S. Kurita, Absorption spectra of anatase TiO2 single crystals heat-treated under oxygen atmosphere, J. Phys. Chem. Solid 61 (2000) 1237–1242, https://doi.org/10.1016/S0022-3697(99)00424-2.
[79] B. Choudhury, A. Choudhury, Oxygen defect dependent variation of band gap, Urbach energy and luminescence property of anatase, anatase–rutile mixed phase and of rutile phases of TiO2 nanoparticles, Physica E Low Dimens Syst Nanostruct. 56 (2014) 364–371, https://doi.org/10.1016/J.PHYSE.2013.10.014.
[80] V.N. Kuznetsov, A.V. Emeline, N.I. Glazkova, R.V. Mikhaylov, N. Serpone, Real-time in situ monitoring of optical absorption changes in visible-light-active TiO2 under light irradiation and temperature-programmed annealing, J. Phys. Chem. C 118 (2014) 27583–27593, https://doi.org/https://doi.org/10.1021/jp5092619.
[81] J. Freitag, A. Domínguez, T.A. Niehaus, A. Hülsewig, R. Dillert, T. Frauenheim, D. W. Bahnemann, Nitrogen(II) oxide charge transfer complexes on TiO2: A new source for visible-light activity, J. Phys. Chem. C 119 (2015) 4488–4501, https://doi.org/https://doi.org/10.1021/jp5108069.
[82] W. Zhou, W. Li, J.Q. Wang, Y. Qu, Y. Yang, Y. Xie, K. Zhang, L. Wang, H. Fu, D. Zhao, Ordered mesoporous black TiO2 as highly efficient hydrogen evolution photocatalyst, J Am Chem Soc. 136 (2014) 9280–9283, https://doi.org/10.1021/JA504802Q/SUPPL_FILE/JA504802Q_SI_001.PDF.
[83] F.S. Eni, C. Oliva, S. Cappelli, Time effects on the stability of the induced defects in TiO2 nanoparticles doped by different nitrogen sources, Article in Journal of Nanoparticle Research. (2012), https://doi.org/10.1007/s11051-012-1301-y.
[84] T. Hirakawa, Y. Nosaka, Selective production of superoxide ions and hydrogen peroxide over nitrogen- and sulfur-doped TiO2 photocatalysts with visible light in aqueous suspension systems, J. Phys. Chem. C 112 (2008) 15818–15823, https://doi.org/https://doi.org/10.1021/jp8055015.
[85] S. Livraghi, M.C. Paganini, E. Giamello, A. Selloni, C. Di Valentin, G. Pacchioni, Origin of photoactivity of nitrogen-doped titanium dioxide under visible light, J Am Chem Soc. 128 (2006) 15666–15671, https://doi.org/10.1021/ja064164c.